

Bessel Functions and Analysis of Circular Waveguides

Jaime Mora-Paz^a, Leszek Demkowicz^a, Christina G. Taylor^a,
Jacob Grosek^b, Stefan Henneking^a

^aOden Institute for Computational Engineering and Sciences, The University of Texas at Austin,
201 E 24th St, Austin, TX, 78712, USA

^bDirected Energy Directorate, Air Force Research Laboratory, 3550 Aberdeen Ave SE,
Albuquerque, NM, 87117, USA

Abstract

The paper is devoted to the study of circularly coiled optical slab waveguides, which is also applicable to acoustical waveguides. We use a change of variables and the classical Frobenius method to compute Bessel functions of complex order and complex argument, and combine it with a perfectly matched layer technique to solve the relevant Bessel eigenvalue problem and deliver accurate loss factors for eigensolutions to the three-layer optical slab waveguide problem. The solutions provide a benchmark for verifying model implementations of this problem and allow for a numerical verification of the Glazman criterion that provides a foundation for the well-posedness and stability analysis of homogeneous circular waveguides with impedance boundary conditions.

Keywords: Bessel functions, circular waveguide, fiber coiling, loss factor, bend loss, PML

AMS classification: 78A50, 35Q61

Acknowledgments

L. Demkowicz, J. Mora-Paz and S. Henneking were supported by AFOSR grant FA9550-23-1-0103.

1 Introduction

Fiber optic waveguides play important roles in many photonic applications, including sensing, scientific experimentation, telecommunications, healthcare, defense technologies, and others. In order to satisfy system spatial restrictions (compact packaging), to control the degree of guidance loss (i.e., differential mode bend loss), and/or to ensure efficient heat dissipation onto a thermally conductive spool/mandrel, these waveguides are typically coiled [28, 25, 19]. Locally, in the coiled regions of the waveguide, the bending can be well approximated to be circular, with a known bend radius. This circular bending affects the propagation of the light through the optical waveguide, especially via mode bend losses. However, accurately predicting these mode bend losses in computer models has remained elusive, in part, because the formulation of the governing system, with reliable boundary conditions, is not even necessarily mathematically well-posed for the three-dimensional electromagnetic waveguide problem.

The present work started as part of an initiative to perform a computational verification of our three-dimensional circularly bent fiber finite element model's methodology [21], implemented in hp3D [13], based on a vectorial envelope formulation [10] of a time-harmonic Maxwell fiber model [11, 12]. To do so, we consider a simplified, circularly bent, two-dimensional (slab) waveguide that has analytic solutions (derived and computed below), even for very slight bends (very large bend radii). This coiled slab waveguide model does not include the *photoelastic effect* [3, 23, 26], where the bending induces a stress/strain that alters the fiber's index of refraction, since this would inhibit the analytic results that we want to compare against. Rather, the main coiling effect on the waveguide arises from the geometry of the circular bend [15, 16, 6], and this is accounted for in our bent slab waveguide problem.

The paper is devoted to a study of the three-layer circular waveguide problem shown in Fig. 1.

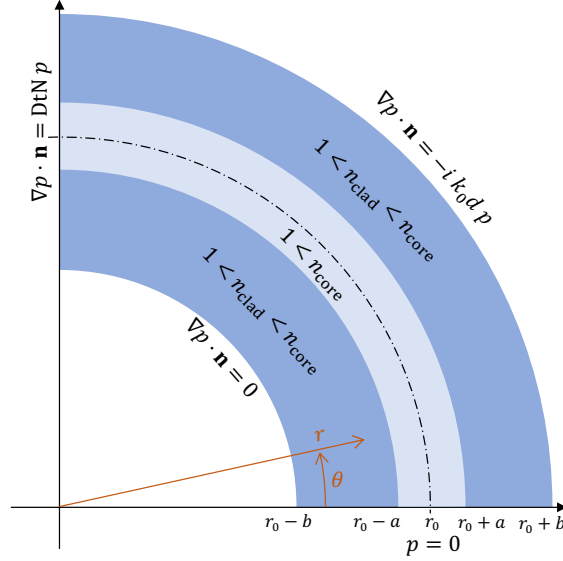


Figure 1: Geometry and boundary conditions for a circular waveguide with a core and a cladding with refractive indices n_{core} and n_{clad} , respectively.

We want to determine the complex-valued scalar field p , satisfying

- Helmholtz equation in the waveguide domain $(r, \theta) \in (r_0 - b, r_0 + b) \times (0, \pi/2)$:

$$\frac{1}{r} \frac{\partial}{\partial r} \left(r \frac{\partial p}{\partial r} \right) + \frac{1}{r^2} \frac{\partial^2 p}{\partial \theta^2} + k_0^2 n^2 p = 0, \quad (1.1)$$

where $n = n(r)$ is the refractive index taking different values in the three layers (either n_{core} or n_{clad} , see Fig. 1);

- interface conditions at $r = r_0 \pm a$:

$$[[p]] = [[\partial p / \partial r]] = 0$$

with $[[\cdot]]$ denoting the jump;

- Neumann boundary condition (BC) at $r = r_0 - b$:

$$\nabla p \cdot \mathbf{n} = 0 ,$$

where \mathbf{n} is the outward unit normal vector;

- impedance (Cauchy or Robin) BC at $r = r_0 + b$:

$$\nabla p \cdot \mathbf{n} = -ik_0 dp ,$$

where $i = \sqrt{-1}$, $k_0 > 0$ denotes the free-space wave number, and $d \geq 0$ represents the strength of the impedance condition; and

- “initial” non-homogeneous Dirichlet BC at $\theta = 0$ (specifying the initial field injected into the waveguide), and a non-local Dirichlet-to-Neumann (DtN) absorbing BC at $\theta = \pi/2$.

The derivations in this paper are made under the convention of a time-harmonic solution of the form $\exp(+i\omega t)p(r, \theta)$, with a known angular frequency $\omega > 0$. Be aware that the leading sign in the exponential implies the sign of some terms of the problem’s equations, particularly in the impedance BC. Now, assuming an ansatz of $p(r, \theta) = \exp(-i\beta\theta)u(r)$, where $\beta \in \mathbb{C}$ is known as the *propagation constant*¹ along the circumferential coordinate θ , we arrive at our governing eigenproblem for the mode $u(r)$ and its eigenvalue $\lambda = \beta^2$:

- Governing mode eigenrelation:

$$r \frac{d}{dr} \left(r \frac{du}{dr} \right) + (\kappa^2 r^2 - \lambda) u = 0 , \quad (1.2)$$

where the wavenumber is $\kappa(r) := k_0 n(r)$. If the medium is homogeneous ($n = n_0 > 0$), then the wavenumber is also a constant, $\kappa = k_0 n_0 > 0$, and the problem becomes a standard Bessel differential equation. This equation can be obtained by rescaling the independent variable, $\tilde{r} := \kappa r$, which implies that

$$\begin{aligned} \frac{d}{dr} &= \kappa \frac{d}{d\tilde{r}} , \quad \frac{d^2}{dr^2} = \kappa^2 \frac{d^2}{d\tilde{r}^2} , \quad r \frac{d}{dr} \left(r \frac{d}{dr} \right) = \tilde{r} \frac{d}{d\tilde{r}} \left(\tilde{r} \frac{d}{d\tilde{r}} \right) , \text{ and so} \\ \tilde{r} \frac{d}{d\tilde{r}} \left(\tilde{r} \frac{du}{d\tilde{r}} \right) + (\tilde{r}^2 - \lambda) u &= 0 . \end{aligned} \quad (1.3)$$

This relation makes it clear that any Bessel solution has an order of $\sqrt{\lambda} = \beta$ and an argument that is scaled by the wavenumber, κ .

- Interface conditions at $r = r_0 \pm a$:

$$\llbracket u \rrbracket = \llbracket \partial u / \partial r \rrbracket = 0 ; \quad (1.4)$$

¹We assume $\text{Re}(\beta) > 0$.

- Neumann boundary condition (BC) at $r = r_0 - b$ ($\mathbf{n} = -\mathbf{e}_r$):

$$\frac{\partial u}{\partial r} = 0; \quad (1.5)$$

- Impedance BC at $r = r_0 + b$ ($\mathbf{n} = \mathbf{e}_r$):

$$\frac{\partial u}{\partial r} + ik_0 u = 0. \quad (1.6)$$

The aim of this paper is to develop a trustworthy procedure to solve the Bessel eigenproblem for three different purposes; namely

- to provide a high accuracy verification for our 3D finite element code implementation for modeling light propagation in bent optical waveguides;
- to numerically verify the Glazman criterion [5] that lays down a theoretical basis for a well-posedness and stability study of circular waveguides; and
- to determine the loss factor, $-\text{Im}(\beta)$, of the propagating modes of a three-layer circular waveguide, using realistic data corresponding to step-index optical fibers, study its dependence upon radius r_0 and compare against results available in the literature [14, 27, 17].

We begin in Section 2 by developing an algorithm based on the classical Frobenius method to compute the Bessel function and its spatial derivative, along with their derivatives with respect to the complex order λ . In Section 3, we numerically verify the Glazman criterion [5] used in the spectral analysis for non-self-adjoint operators to provide some support for the well-posedness to our approach. Our proposed algorithm to solve the actual three-layer eigenvalue problem is delineated in Section 4, along with numerical results. Next, in Section 5, we replace the impedance BC with a perfectly matched layer (PML) and study the effect of the PML parameters on the propagation constant β . Finally, in Section 6, we use our methodology to estimate the losses induced by the bending and compare it with loss formulas available in the literature.

REMARK 1 There are two possibilities to physically interpret problem (1.1) and its boundary conditions. On one hand, p may represent the pressure in time-harmonic acoustical waves, with a *sound hard* BC on the inner boundary. Alternatively, a derivation from Maxwell's equations, under the assumptions of no free charges, no material magnetic susceptibility, and a linearly polarized electric field in a direction perpendicular to the plane (r, θ) , yields an identical scalar eigenproblem, where p corresponds to such a component of the time-harmonic electric field, \mathbf{E} . Its BC on the left-hand end is interpreted as a *magnetic* BC. Additionally, the impedance BC in the scalar problem can be shown to be equivalent to the impedance BC for electromagnetics. In the latter, the tangential components of \mathbf{E} and the magnetic field \mathbf{H} hold the following relationship:

$$Z_{\text{clad}} \mathbf{n} \times (\mathbf{H} \times \mathbf{n}) + \mathbf{E} \times \mathbf{n} = \mathbf{0}, \quad (1.7)$$

where Z_{clad} is the impedance of the cladding (outer layer), given by $Z_{\text{clad}} = Z/n_{\text{clad}}$, where Z is the free-space impedance, $Z := \sqrt{\mu_0/\epsilon_0}$, which is a function of the free-space permittivity ϵ_0 and free-space permeability μ_0 . Since $\mathbf{n} = \mathbf{e}_r$ on the impedance boundary (see Fig. 1), BC (1.7) is equivalent to (1.6) because

$$\begin{aligned} \dots \text{the } \theta\text{-component of (1.7) implies that} & \quad \frac{1}{n_{\text{clad}}} \sqrt{\frac{\mu_0}{\epsilon_0}} H_\theta + p = 0; \\ \dots \text{by Faraday's law, } i\omega\mu_0\mathbf{H} = -\nabla \times \mathbf{E} \text{ implies that} & \quad \frac{1}{n_{\text{clad}}} \sqrt{\frac{\mu_0}{\epsilon_0}} \frac{1}{i\omega\mu_0} \frac{\partial p}{\partial r} + p = 0; \text{ and} \\ \dots \text{using } \omega = k_0/\sqrt{\epsilon_0\mu_0} \text{ implies that} & \quad \frac{\partial p}{\partial r} + \underbrace{ik_0 n_{\text{clad}}}_{ik_0 d} p = 0. \end{aligned}$$

■

2 Evaluation of Bessel functions of large argument and large complex order

A significant computational problem arises in the simplest version of the three-layer circular waveguide, where $n = n_0 > 0$, because the eigenfunctions (i.e., waveguide modes) are solved with Bessel functions whose orders are dependent on the complex-valued eigenvalues (cf. the Bessel eigenproblem (1.3)). Furthermore, these eigenvalues scale with the bend radius (r_0) according to $\lambda \sim r_0^2$. Thus, for slight waveguide bends (i.e., large bend radii), the eigensolutions involve evaluating Bessel functions with both large arguments and large complex orders, for which maintaining sufficient precision is not a trivial task.

Consider dividing equation (1.3) by r_0^2 :

$$\begin{aligned} \frac{\tilde{r}}{r_0} \frac{d}{d\tilde{r}} \left(\frac{\tilde{r}}{r_0} \frac{du}{d\tilde{r}} \right) + \left(\frac{\tilde{r}^2}{r_0^2} - \frac{\lambda}{r_0^2} \right) u &= 0 \\ \frac{r}{r_0} \frac{d}{dr} \left(\frac{r}{r_0} \frac{du}{dr} \right) + \left(k_0^2 n_0^2 \left(\frac{r}{r_0} \right)^2 - \frac{\lambda}{r_0^2} \right) u &= 0 \text{ for } r \in (r_0 - b, r_0 + b). \end{aligned} \quad (2.1)$$

We wish to rescale the problem in such a way that we can solve it for $\mu := \lambda/r_0^2$. This can be accomplished with a substitution of the independent variable (cf. conformal mapping technique [9]):

$$x := r_0 \ln \left(\frac{r}{r_0} \right), \quad (2.2)$$

which implies that

$$\frac{r}{r_0} = \exp \left(\frac{x}{r_0} \right) \quad \text{and} \quad \frac{r}{r_0} \frac{du}{dr} = \frac{r}{r_0} \frac{du}{dx} \frac{dx}{dr} = \frac{r}{r_0} \frac{du}{dx} r_0 \frac{1}{r} = \frac{du}{dx}.$$

This transforms the Bessel differential equation (2.1) into

$$\frac{d^2 u}{dx^2} + \left(\kappa^2 \exp \left(\frac{2x}{r_0} \right) - \mu \right) u = 0 \quad \text{for } x \in \left(r_0 \ln \left(\frac{r-b}{r_0} \right), r_0 \ln \left(\frac{r+b}{r_0} \right) \right). \quad (2.3)$$

The geometric effect induced by the circular bend is represented by the $\exp(2x/r_0)$ factor.

Since the thickness of the waveguide is always much smaller than the bend radius, $b \ll r_0$, then $r \approx r_0$, which means that $x \approx 0$. Using a Taylor expansion about $x = 0$, $\exp(2x/r_0) \approx 1$, and so

$$\frac{d^2 u}{dx^2} + (\kappa^2 - \mu) u = \frac{d^2 u}{dx^2} + (k_0^2 n_0^2 - \mu) u \simeq 0 ,$$

which is approximately the eigenproblem for a straight waveguide with μ as the mode eigenvalue. Indeed, in the limit as $r_0 \rightarrow \infty$, the waveguide is no longer circularly coiled, and the eigenproblem converges to

$$\frac{d^2 u}{dx^2} + (k_0^2 n_0^2 - \mu) u = 0 \quad \text{for } x \in (-b, b) \quad (\text{cf. relation (4.6)})$$

because

$$\lim_{r_0 \rightarrow \infty} r_0 \ln \left(\frac{r_0 \pm b}{r_0} \right) = \pm b .$$

Using typical parameters and design properties for optical fiber waveguides (see Section 4), when $\kappa^2 \approx 4.74 \cdot 10^4$ and $r_0^2 = 1.69 \cdot 10^8$, with $-5 \leq x \leq 5$ (in non-dimensional units), implies that $0.99923 \leq \exp(2x/r_0) \leq 1.00076$. Such small perturbations from unity imply that, in order to compute a proper solution of the Bessel eigenequation (2.3) for large bend radii, it becomes imperative to work with floating-point arithmetic of high levels of precision. By using our procedures along with “arbitrary” (user-requested) precision floating-point arithmetic, we are able to provide semi-analytical solutions to Bessel’s differential equation corresponding to the bent waveguide problems herein described.

Computation of the rescaled Bessel functions. The Frobenius method for evaluating a Bessel function seeks a solution of the form

$$u(x) = \sum_{m=0}^{\infty} c_m x^m . \quad (2.4)$$

We use the Taylor expansion for the variable factor $\exp(2x/r_0)$ about $x = 0$:

$$\exp \left(\frac{2x}{r_0} \right) = \sum_{l=0}^{\infty} \frac{2^l}{r_0^l l!} x^l .$$

Using these two expansions in our transformed Bessel differential equation (2.3), followed by a reorganization of the power series, we obtain the following explicit recursion relation for the coefficients, c_n , for the Bessel solution of order μ :

$$(m+1)(m+2)c_{m+2} + \kappa^2 \sum_{l=0}^m \frac{2^{m-l}}{r_0^{m-l} (m-l)!} c_l - \mu c_m = 0 \quad \text{for } m \in \mathbb{N} . \quad (2.5)$$

Note that this recursion specifies the solution up to two constants: c_0 and c_1 , which are both free parameters. Let the functions $V_\mu(x)$ and $W_\mu(x)$ be defined by the recursion relation constants obtained from (2.5) when choosing $c_0 = 1, c_1 = 0$ and $c_0 = 0, c_1 = 1$, respectively. Specifically, the

constants coincide with the value of the solution and its derivative at $x = 0$ such that the recursion generates a two-parameter family of solutions:

$$u(x) = CV_\mu(x) + DW_\mu(x), \quad C, D \in \mathbb{C}. \quad (2.6)$$

Note that our functions $V_\mu(x(r))$, $W_\mu(x(r))$ are two linearly independent solutions to the Bessel equation (1.2). As such, they span the same solution space as the classical pair of Bessel functions of the first and second kind $(J_\beta(\kappa r), Y_\beta(\kappa r))$, or the pair of Hankel functions of the first and second kind $(H_\beta^{(1)}(\kappa r), H_\beta^{(2)}(\kappa r))$. We stress the point that implementing custom solutions allows for a computationally efficient and arbitrarily precise evaluation of Bessel functions of large complex order and large argument, which is a major challenge when using standard software packages to evaluate the Bessel and Hankel functions.²

The present algorithm can be used to compute Bessel functions in two different contexts:

- **Evaluation of particular solutions to Bessel's equation:** if μ is known, for a given r we evaluate the two fundamental solutions $V_\mu(x(r))$ and $W_\mu(x(r))$, truncating the series whenever the two latest increments $|c_m x^m|$ are below the desired precision. Moreover, if C and D are provided, we can deliver the value of the particular solution (2.6).
- **Bessel's eigenvalue equation solver:** If we seek the eigenvalue μ and the eigenfunction (or mode profile), $u(x(r))$, which needs to satisfy two certain homogeneous BCs, we use an iterative nonlinear solver to determine C , D and μ . A scaling condition (such as requiring $u(x(r_0 - b)) = 1$ or setting one of the coefficients to unity) completes the system. By using appropriate algebraic manipulation, this 3-by-3 nonlinear system may be reduced to a 2-by-2 system or even to a single nonlinear equation depending on the eigenvalue. Using the propagation constants of the corresponding straight waveguide problem for the initial guess of the eigenvalue is typically an effective method to converge to the desired value of μ . With this setup, we need only evaluate V_μ and W_μ (and their derivatives) at the endpoints, making it an efficient and accurate method to determine the eigenvalues and modes of the problem.

Derivative of the rescaled Bessel function with respect to order μ . When implementing a nonlinear solver for finding the eigenvalues and modes, it is be prudent to examine the derivatives of the governing eigenproblem (2.3) with respect to the order. By differentiating with respect to the eigenvalue μ , one obtains a non-homogeneous Bessel relation:

$$\frac{\partial^2}{\partial x^2} \left[\frac{\partial u}{\partial \mu} \right] + \left(\kappa^2 \exp \left(\frac{2x}{r_0} \right) - \mu \right) \frac{\partial u}{\partial \mu} = u, \quad (2.7)$$

²To observe the difficulty of evaluating Bessel functions of large complex order and large argument first-hand, an exercise suggested to the reader consists of trying to draw a plot (with the mathematical software of their choice) of $J_\beta(\kappa r)$ for $r \in [r_0 - b, r_0 + b]$, with $r_0 = 10^4$, $b = 1$, $\kappa = 10^2$, $\beta = \sqrt{10^{12} - 100i}$, and assessing the speed of the computation and its sensitivity to small variations in β .

where u is still the solution of (2.3), corresponding to particular constants c_0, c_1 . However, we will now presume that $\partial u / \partial \mu$ can be well represented in terms of a new series expansion,

$$\frac{\partial u}{\partial \mu} = \sum_{m=0}^{\infty} b_m x^m.$$

By uniqueness of the power series, we can deduce that $b_m = \partial c_m / \partial \mu$. Note that both b_0 and b_1 vanish, which is a consequence of the fact that coefficients c_0 and c_1 are fixed independently of the value of μ . Inserting this expansion into (2.7) produces a recursion relation for the coefficients, b_m :

$$b_0 = b_1 = 0; \quad (m+1)(m+2)b_{m+2} + \kappa^2 \sum_{l=0}^m \frac{2^{m-l}}{r_0^{m-l}(m-l)!} b_l - \mu b_m = c_m \quad \text{for } m \in \mathbb{N}, \quad (2.8)$$

where we compute the terms of the power series until the desired precision is reached.

The partial derivative of (2.6) with respect to μ is given by

$$\frac{\partial u}{\partial \mu} = C \frac{\partial V_\mu}{\partial \mu}(x) + C \frac{\partial W_\mu}{\partial \mu}(x). \quad (2.9)$$

Above, $\partial V_\mu / \partial \mu$ is obtained by computing b_m with the resulting sequence (2.5) started by $c_0 = 1$, $c_1 = 0$, while $\partial W_\mu / \partial \mu$ uses the c_m sequence that begins with $c_0 = 0$, $c_1 = 1$. Differentiating the polynomial expansion for $\partial u / \partial \mu$ with respect to x yields

$$\frac{\partial}{\partial x} \left[\frac{\partial u}{\partial \mu} \right] = \frac{\partial}{\partial \mu} \left[\frac{\partial u}{\partial x} \right] = \sum_{m=2}^{\infty} m b_m x^{m-1} = \sum_{m=1}^{\infty} (m+1) b_{m+1} x^m.$$

By combining $\partial u / \partial \mu$ and $\partial / \partial \mu [\partial u / \partial x]$, evaluated at each endpoint, along with partial derivatives of u and $\partial u / \partial x$ with respect to C and D , we obtain the Jacobian of the nonlinear system consisting of the two BC operators and the scaling condition, all of which depend on μ and the coefficients, so that we can iteratively solve it with the Newton–Raphson method.

To illustrate how this algorithm for finding the eigensolution is used, we present two applications. First, in Section 3, the homogeneous circularly coiled waveguide is solved, subject to the impedance BC (1.6) on the outer boundary. Second, the described algorithm is utilized to analyze the three-layer circularly bent waveguide, which additionally must satisfy the interface conditions (1.4). The intricate treatment of the piecewise solution and the interface conditions is delineated in Section 4.

3 First application: Numerical evidence for the spectral analysis of a circular waveguide with impedance BC

In [5], the authors studied the well-posedness and stability of a straight acoustical waveguide with impedance BC. Using separation of variables, the solution is expanded into a set of modes (eigenfunctions). The non-triviality of the problem lies in the fact that—contrary to the homogeneous waveguide with sound hard BC [20]—the operator that defines the modes here is *not* self-adjoint;

hence the modes are orthogonal neither in the L^2 , nor in the H^1 , inner product. Thus, the completeness of the modes in the L^2 and H^1 spaces no longer follows from the Sturm–Liouville theory (cf. Spectral Theorem for Self-Adjoint Operators). Rather, non-self-adjoint operator theory must be employed, as discussed in reference [7]. The proof of well-posedness relies upon the Glazman Theorem (see p. 328 of [7]), which requires the verification of the Glazman condition expressed in terms of the eigenvalues, λ_n :

$$\sum_{\substack{i,j=1 \\ i \neq j}}^{\infty} \frac{\text{Im}(\lambda_i) \text{Im}(\lambda_j)}{|\lambda_i - \lambda_j|^2} < \infty. \quad (3.1)$$

Note that this condition is trivially satisfied for the waveguide problem with hard or soft BCs for which the operator is self-adjoint, which enforces real-valued eigenvalues; hence $\text{Im}(\lambda_j) = 0$, $\forall j$. However, for the straight waveguide with impedance BC, the eigenproblem leads to a transcendental equation involving the tangent function with complex variables, which can be manipulated to study the behavior of the equation’s roots (i.e., the problem’s eigenvalues) and thereby the satisfaction of the Glazman criterion (3.1).

In the present application, we return to a homogeneous circular waveguide (setting $n(r) = 1$), with a Neumann BC on the inner boundary, $u(r_0 - b) = 0$, and the impedance BC (1.6) on the outer boundary, and we numerically study the behavior of the first 30 eigenvalues of (2.3). Since the Bessel eigenvalue equation with impedance BC can be regarded as a non-self-adjoint operator as well, we aim to computationally check whether the Glazman criterion is also satisfied for the case of a bent waveguide.

Fig. 2 depicts the computational results for $n = 1, 2, \dots, 30$, with parameters $\kappa = 10$, $r_0 = 100$, $b = 0.5$, and $d = 1$. We show the real (plot a) and imaginary (plot b) components of the function

$$\alpha_n(\lambda_n) := \sqrt{\kappa^2 - \frac{\lambda_n}{r_0^2}}, \quad (3.2)$$

as well as the finite sums (plot c) of the Glazman condition (3.1),

$$G_n = \sum_{\substack{i,j=1 \\ i \neq j}}^n \frac{\text{Im}(\lambda_i) \text{Im}(\lambda_j)}{|\lambda_i - \lambda_j|^2}, \quad n = 1, 2, \dots \quad (3.3)$$

For large r_0 , and $d = 0$, the straight waveguide analysis from [5] indicates that

$$-\lambda_n \cong r_0^2 (-\kappa^2 + (n\pi)^2).$$

So, for a large bend radius and a low impedance value, one would expect that $n\pi \cong \alpha_n$. We use this relation to generate initial guesses for the real component of the eigenvalues. After a small pre-asymptotic region, analogous to propagating modes in the straight waveguide, the real part of α_n coincides with $n\pi$ up to the first five significant digits. At the same time, the imaginary part of α_n converges to zero, asymptotically following the rule $-2bd\kappa/(\pi n)$; cf. [5, Lemma 2]. The third plot displays the finite sums G_n computed by (3.3); here, the sum converging to a finite limit, supporting the hypothesis that condition (3.1) holds and, hence, the well-posedness of the problem should be expected.

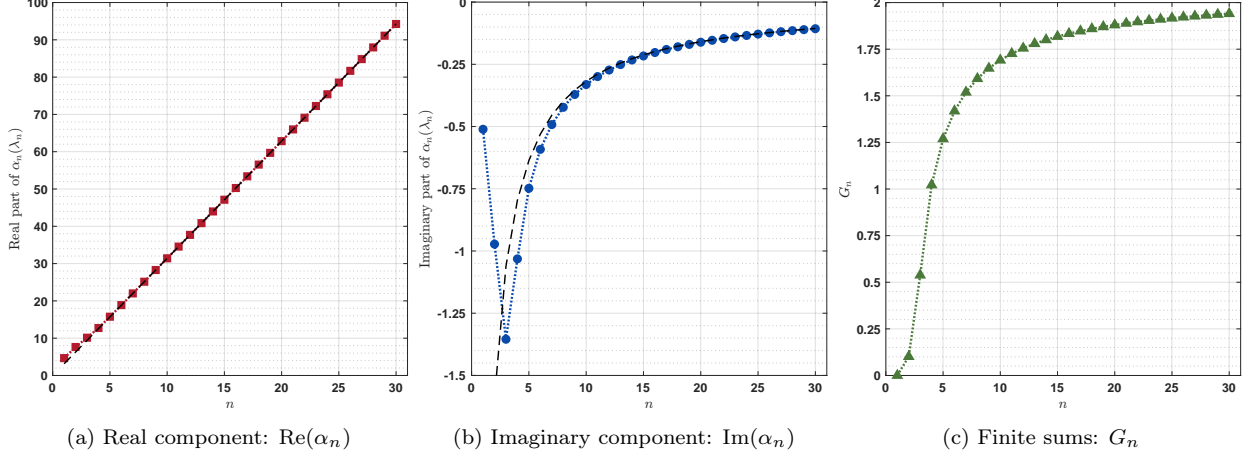


Figure 2: The real (plot **a**) and imaginary (plot **b**) components of the $\alpha_n = \alpha_n(\lambda_n)$ function (3.2) for the first 30 eigenvalues of (2.3) using $n_0 = 1$, $\kappa = 10$, $r_0 = 100$, $b = 0.5$, and $d = 1$. According to the theoretical results in [5], in the limit of a straight waveguide ($r_0 \rightarrow \infty$), $\text{Re}(\alpha_n) \rightarrow n\pi$ and $\text{Im}(\alpha_n) \rightarrow -2bd\kappa/(\pi n)$ (see the black dashed lines in **a** and **b**). In plot **c**, we present the finite sums G_n (3.3) associated with Glazman condition (3.1), observing the convergence of the series.

4 Main application: Three-layer circular waveguide eigenproblem

Next, we solve the three-layer waveguide eigenproblem in the x coordinate. The solution consists of three branches corresponding to the core and the two (left and right) cladding regions. The solution in the waveguide core region will be represented as a function of x , with $x = 0$ corresponding to $r = r_0$; the solution in the left cladding region, $r < r_0 - a$, will be represented as a function of x_1 , such that $x_1 = 0$ corresponds to $r = r_0 - a$; and the solution in the right cladding region, $r > r_0 + a$, will be represented as a function of x_2 , such that $x_2 = 0$ corresponds to $r = r_0 + a$. The logarithmic transformation of x is as presented in Section 2, while for x_1 and x_2 we change the base point r_0 to $r_0 - a$ and $r_0 + a$, respectively:

$$x_1(r) := (r_0 - a) \ln \left(\frac{r}{r_0 - a} \right), \quad x(r) := r_0 \ln \left(\frac{r}{r_0} \right) \quad (\text{cf. 2.2}), \quad \text{and} \quad x_2(r) := (r_0 + a) \ln \left(\frac{r}{r_0 + a} \right).$$

The regional interfaces/boundaries occur at

$$\begin{aligned} -b_1 &:= (r_0 - a) \ln \left(\frac{r_0 - b}{r_0 - a} \right), & -a_1 &:= r_0 \ln \left(\frac{r_0 - a}{r_0} \right), \\ a_2 &:= r_0 \ln \left(\frac{r_0 + a}{r_0} \right), & \text{and } b_2 &:= (r_0 + a) \ln \left(\frac{r_0 + b}{r_0 + a} \right). \end{aligned}$$

The wavenumber κ for the left ($r < r_0 - a$) and right ($r > r_0 + a$) cladding regions is $\kappa_{\text{clad}} = k_0 n_{\text{clad}}$, whereas for the core region it is $\kappa_{\text{core}} = k_0 n_{\text{core}}$. Likewise, the eigenvalues μ become regionally defined:

$$\begin{cases} \mu_1 := \lambda/(r_0 - a)^2 & \text{for } x_1(r) \in [-b_1, 0], \\ \mu := \lambda/r_0^2 & \text{for } x(r) \in [-a_1, a_2], \\ \mu_2 := \lambda/(r_0 + a)^2 & \text{for } x_2(r) \in [0, b_2]. \end{cases}$$

As an ansatz, the solution is presumed to take the form

$$u(r) = \begin{cases} u^{\text{left}}(x_1(r)) = C_1 V_{\mu_1}^{\text{left}}(x_1(r)) + D_1 W_{\mu_1}^{\text{left}}(x_1(r)) & \text{for } x_1(r) \in [-b_1, 0], \\ u^{\text{core}}(x(r)) = C_0 V_{\mu}^{\text{core}}(x(r)) + D_0 W_{\mu}^{\text{core}}(x(r)) & \text{for } x(r) \in [-a_1, a_2], \\ u^{\text{right}}(x_2(r)) = C_2 V_{\mu_2}^{\text{right}}(x_2(r)) + D_2 W_{\mu_2}^{\text{right}}(x_2(r)) & \text{for } x_2(r) \in [0, b_2], \end{cases} \quad (4.1)$$

where the functions V_{μ} and W_{μ} are computed with (2.4)–(2.5), with the specifications detailed in Table 1. It is important to make sure that the substitution of the base point r_0 to either $r_0 - a$ or $r_0 + a$ (according to the cladding region), is taken into account not only when evaluating x_1 or x_2 but also within the recursions (2.5) and (2.8).

Table 1: Detailed description of the argument and parameters corresponding to the evaluation of the custom fundamental Bessel solutions V_{μ} and W_{μ} , calculated through (2.4)–(2.5), required to construct the piecewise solution (4.1).

Function V_{μ} or W_{μ}	Argument and parameters to evaluate					
	$x \leftarrow$	$r_0 \leftarrow$	$\kappa \leftarrow$	$\mu \leftarrow$	$c_0 \leftarrow$	$c_1 \leftarrow$
$V_{\mu_1}^{\text{left}}$	$x_1(r)$	$r_0 - a$	κ_{clad}	μ_1	1	0
$W_{\mu_1}^{\text{left}}$	$x_1(r)$	$r_0 - a$	κ_{clad}	μ_1	0	1
V_{μ}^{core}	$x(r)$	r_0	κ_{core}	μ	1	0
W_{μ}^{core}	$x(r)$	r_0	κ_{core}	μ	0	1
$V_{\mu_2}^{\text{right}}$	$x_2(r)$	$r_0 + a$	κ_{clad}	μ_2	1	0
$W_{\mu_2}^{\text{right}}$	$x_2(r)$	$r_0 + a$	κ_{clad}	μ_2	0	1

Treatment of interface and boundary conditions. The interface conditions (1.4) are

$$u^{\text{left}}(0) = u^{\text{core}}(-a_1) \quad \text{and} \quad u^{\text{right}}(0) = u^{\text{core}}(a_2), \quad (4.2)$$

and (note the change of variable)

$$\frac{du^{\text{left}}}{dx_1}(0) = \frac{r_0}{r_0 - a} \frac{du^{\text{core}}}{dx}(-a_1) \quad \text{and} \quad \frac{du^{\text{right}}}{dx_2}(0) = \frac{r_0}{r_0 + a} \frac{du^{\text{core}}}{dx}(a_2). \quad (4.3)$$

Finally, the Neumann BC (1.5) at $x_1 = -b_1$ is formulated as

$$\frac{r_0 - a}{r_0 - b} \frac{du^{\text{left}}}{dx_1}(-b_1) = 0, \quad (4.4)$$

and the impedance BC (1.6) at $x_2 = b_2$ is given by

$$\frac{r_0 + a}{r_0 + b} \frac{du^{\text{right}}}{dx_2}(b_2) + i\kappa_{\text{clad}} du^{\text{right}}(b_2) = 0. \quad (4.5)$$

Detailed description of the eigenvalue solver for a circularly bent three-layer waveguide.

For our study, we seek two types of eigensolutions (4.1):

- *Even* modes, where $C_0 \equiv 1$ and D_0 needs to be determined; and

- *Odd* modes, where $D_0 \equiv 1$ and C_0 needs to be determined.

We evaluate the solution and its derivative at $x \in \{-a_1, a_2\}$ and use interface conditions (4.2)–(4.3) to generate the corresponding solutions in the two cladding regions. In other words, constants C_1, D_1, C_2, D_2 are determined on-the-fly using (4.2)–(4.3), so that u^{left} and u^{right} can be constructed and evaluated. Finally, enforcing BCs (4.4)–(4.5) leads to a system of two nonlinear equations for unknowns $\{D_0, \lambda\}$ (when seeking even modes), or $\{C_0, \lambda\}$ (when seeking odd modes).

For example, considering an even mode ($C_0 \equiv 1$), we start by imposing the zero-valued Neumann BC on the inside of the bend and the impedance BC on the outside of the bend:

$$\begin{cases} \text{BC}_{\text{inner}}(D_0, \lambda) := \frac{\partial u^{\text{left}}}{\partial x_1}(-b_1) = 0 \quad (\text{cf. 1.5}), \quad \text{and} \\ \text{BC}_{\text{outer}}(D_0, \lambda) := \frac{r_0 + a}{r_0 + b} \frac{du^{\text{right}}}{dx_2}(b_2) + ik_0 du^{\text{right}}(b_2) = 0 \quad (\text{cf. 4.5}). \end{cases}$$

This nonlinear system $(\text{BC}_{\text{inner}}, \text{BC}_{\text{outer}})$ is solved for D_0 and λ numerically using the Newton–Raphson method, requiring the derivatives of the two functions BC_{inner} and BC_{outer} . Starting with BC_{inner} , using its expression from (4.1), we find that

$$\begin{aligned} \frac{\partial u^{\text{left}}}{\partial x_1}(-b_1) &= C_1 \frac{\partial V_{\mu_1}^{\text{left}}}{\partial x_1}(-b_1) + D_1 \frac{\partial W_{\mu_1}^{\text{left}}}{\partial x_1}(-b_1) \\ &= u^{\text{left}}(0) \frac{\partial V_{\mu_1}^{\text{left}}}{\partial x_1}(-b_1) + \frac{du^{\text{left}}}{dx_1}(0) \frac{\partial W_{\mu_1}^{\text{left}}}{\partial x_1}(-b_1) \\ &= u^{\text{core}}(-a_1) \frac{\partial V_{\mu_1}^{\text{left}}}{\partial x_1}(-b_1) + \frac{r_0}{r_0 - a} \frac{du^{\text{core}}}{dx}(-a_1) \frac{\partial W_{\mu_1}^{\text{left}}}{\partial x_1}(-b_1), \end{aligned}$$

where

$$u^{\text{core}}(-a_1) = C_0 V_{\mu}^{\text{core}}(-a_1) + D_0 W_{\mu}^{\text{core}}(-a_1) \quad \text{and} \quad \frac{du^{\text{core}}}{dx}(-a_1) = C_0 \frac{dV_{\mu}^{\text{core}}}{dx}(-a_1) + D_0 \frac{dW_{\mu}^{\text{core}}}{dx}(-a_1).$$

Differentiating these two formulas with respect to constant D_0 , we obtain

$$\frac{\partial}{\partial D_0} [u^{\text{core}}(-a_1)] = W_{\mu}^{\text{core}}(-a_1) \quad \text{and} \quad \frac{\partial}{\partial D_0} \left[\frac{du^{\text{core}}}{dx}(-a) \right] = \frac{dW_{\mu}^{\text{core}}}{dx}(-a_1).$$

Hence,

$$\frac{\partial}{\partial D_0} \left[\frac{\partial u^{\text{left}}}{\partial x_1}(-b_1) \right] = W_{\mu}^{\text{core}}(-a_1) \frac{dV_{\mu_1}}{dx_1}(-b_1) + \frac{r_0}{r_0 - a} \frac{dW_{\mu}^{\text{core}}}{dx}(-a_1) \frac{dW_{\mu_1}}{dx_1}(-b_1).$$

Similarly, but now differentiating with respect to the other unknown, λ , one finds that

$$\begin{aligned}
\frac{\partial}{\partial \lambda} \left[\frac{\partial u^{\text{left}}}{\partial x_1}(-b_1) \right] &= \frac{\partial}{\partial \lambda} [u^{\text{core}}(-a_1)] \frac{dV_{\mu_1}}{dx_1}(-b_1) + \frac{r_0}{r_0 - a} \frac{\partial}{\partial \lambda} \left[\frac{du^{\text{core}}}{dx}(-a_1) \right] \frac{dW_{\mu_1}}{dx_1}(-b_1) \\
&\quad + u^{\text{core}}(-a_1) \frac{\partial}{\partial \lambda} \left[\frac{dV_{\mu_1}}{dx_1}(-b_1) \right] + \frac{r_0}{r_0 - a} \frac{du^{\text{core}}}{dx}(-a_1) \frac{\partial}{\partial \lambda} \left[\frac{dW_{\mu_1}}{dx_1}(-b_1) \right] \\
&= \frac{1}{r_0^2} \left(\frac{\partial}{\partial \mu} [u_{\mu}(-a_1)] \frac{dV_{\mu_1}}{dx_1}(-b_1) + \frac{r_0}{r_0 - a} \frac{\partial}{\partial \mu} \left[\frac{du_{\mu}}{dx}(-a_1) \right] \frac{dW_{\mu_1}}{dx_1}(-b_1) \right) \\
&\quad + \frac{1}{(r_0 - a)^2} \left(u^{\text{core}}(-a_1) \frac{\partial}{\partial \mu_1} \left[\frac{dV_{\mu_1}^{\text{left}}}{dx_1}(-b_1) \right] \right. \\
&\quad \left. + \frac{r_0}{r_0 - a} \frac{u^{\text{core}}}{x}(-a_1) \frac{\partial}{\partial \mu_1} \left[\frac{dW_{\mu_1}^{\text{left}}}{dx_1}(-b_1) \right] \right)
\end{aligned}$$

where

$$\begin{aligned}
\frac{\partial}{\partial \mu} [u^{\text{core}}(-a_1)] &= C_0 \frac{\partial V_{\mu}^{\text{core}}}{\partial \mu}(-a_1) + D_0 \frac{\partial W_{\mu}^{\text{core}}}{\partial \mu}(-a_1) \quad \text{and} \\
\frac{\partial}{\partial \mu} \left[\frac{du^{\text{core}}}{dx}(-a_1) \right] &= C_0 \frac{\partial}{\partial \mu} \left[\frac{dV_{\mu}^{\text{core}}}{dx}(-a_1) \right] + D_0 \frac{\partial}{\partial \mu} \left[\frac{dW_{\mu}^{\text{core}}}{dx}(-a_1) \right].
\end{aligned}$$

The formulas for derivatives with respect to μ presented in Section 2 prove helpful for implementing these just-derived expressions.

Analogously, one determines the formulas for the derivatives of BC_{outer} with respect to the unknowns D_0 and λ , so that the Newton method can use those formulas in its calculations. In the case of an odd mode, we require the partial derivatives $\partial/\partial C_0$ instead of $\partial/\partial D_0$, because in that case C_0 is the unknown while $D_0 = 1$ is fixed.

Nondimensionalization. The physical scales involved in the three-layer optical waveguide model, when expressed in SI units (see Table 3), range over 26 orders of magnitude. With sagacious choices for the characteristic sizes of the length, mass, time, and electrical current parameters, we can reduce this range to 6 orders of magnitude. The practical length unit is taken to match the waveguide's core diameter of 25.4 microns (10^{-6} m), while the rest are chosen to get the magnitude of most parameters closer to 1, as shown in Table 2. By normalizing with these four fundamental quantities, we can nondimensionalize the entire problem since the other derived units involved, such as Newton (N), Volt (V) and Farad (F), can be expressed in terms of the four units given (m, kg, s, A).

Table 2: Characteristic sizes used for the nondimensionalization of the governing system.

Reference length	$25.4 \cdot 10^{-6}$ m
Reference mass	10^{-22} kg
Reference time	10^{-13} s
Reference electrical current	400 A

From this point onward, all parameter values will be presented in their nondimensional form without notationally distinguishing them from their dimensional counterparts.

Table 3: Coiled waveguide parameters in both SI and nondimensional units. All the waveguide’s properties are adapted from the optical step-index fiber analyzed in [11].

Parameter	Symbol	Value in SI Units	Nondimensionalized Value
Bend radius range	r_0	$[0.03302 \text{ m}, 0.3302 \text{ m}]$	$\in [1300, 13000]$
Core’s half-width	a	$1.27 \cdot 10^{-5} \text{ m}$	0.5
Cladding’s half-width	b	$1.27 \cdot 10^{-4} \text{ m}$	5.0
Core’s refractive index	n_0	1.4512	1.4512
Cladding’s refractive index	n_1	1.45	1.45
Impedance BC strength	d	1.45	1.45
Free-space wavenumber	k_0	$5.905 \cdot 10^6 \text{ rad/m}$	$1.49993333460866 \cdot 10^2$
Angular frequency	ω	$1.77035 \cdot 10^{15} \text{ rad/s}$	$1.77034921739554 \cdot 10^2$
Vacuum permeability	μ_0	$1.25664 \cdot 10^{-6} \text{ N/A}^2$	0.791582400800000
Vacuum permittivity	ϵ_0	$8.85419 \cdot 10^{-12} \text{ F/m}$	0.906838390340768
Free-space impedance	Z	$3.76730313412 \cdot 10^2 \text{ V/A}$	0.934293045847926

On the computational implementation and the precision digits. Since we are aware that the expected eigenvalues demand an outstanding accuracy, the methodology explained above has been translated to high-precision scientific computing codes in both Fortran and the Julia language [2].

In Fortran, we have used the 128-bit floating-point variables (quadruple precision). With those variables it is possible to handle floating-point arithmetic with up to thirty-four digits of precision, so we choose to enforce a precision of 10^{-32} in the Bessel-Frobenius power series convergence, and at most 10^{-29} for the eigenvalue convergence. Only the results presented in Section 3 and in Table 4 are calculated with our Fortran implementation.

On the other hand, in the Julia implementation, thanks to the MPFR library, originally developed in C, arbitrary floating-point precision is attainable. The results provided in this paper are computed with a 70-decimal-digit setup, with a Bessel power series tolerance of 10^{-65} and the eigenvalue tolerance set to 10^{-60} . The maximum number of terms in the power series is set to 1000, and the maximum number of Newton iterations is 50. Extending to a more demanding precision level is straightforward, without a dramatic performance penalization.

Since one of the goals of the present research effort is to obtain benchmarking solutions for a finite element software implemented in double precision, the main results in the tables below are delivered in a fifteen-digit format, so that it can be more directly translated to a double-precision implementation of the basic algorithm (which does not require finding the eigenvalues, but rather to just compute and combine the two fundamental solutions of the Bessel-Frobenius power series with a given μ).

How to interpret the numerical results. In the tables of this section and the next section we report the eigenvalue λ , the propagation constant $\beta = \sqrt{\lambda}$ and the result $\beta/r_0 = \sqrt{\mu}$. Although λ

has no direct physical meaning, after rewriting our initial ansatz for the scalar field,

$$p(r, \theta) = \exp(-i\beta\theta)u(r) = \underbrace{\exp(-i \operatorname{Re}(\beta)\theta)}_{\text{harmonic}} \underbrace{\exp(\operatorname{Im}(\beta)\theta)}_{\text{decays if } \operatorname{Im}(\beta) < 0} u(r) = \exp\left(-i \frac{\beta}{r_0} \underbrace{r_0\theta}_{\approx \text{longitudinal coordinate}}\right) u(r),$$

we note the following:

1. The propagation constant β , which is multiplied by the angle θ in radians, is nondimensional. Its real part induces a harmonic function in the circumferential direction.
2. In contrast, the imaginary part of β , if negative, causes an exponential decay in the value of $u(r)$. More precisely, we interpret $-\operatorname{Im}(\beta)$ as the amplitude loss factor per radian. If $\operatorname{Im}(\beta)$ is very close to zero, the coiling losses are not significant, but if, for instance, $-\operatorname{Im}(\beta) = 0.01$, a single turn (2π radians) causes a loss of $1 - \exp(-0.01 \cdot 2\pi) \approx 6.1\%$, whereas 50 coils induce a loss of $1 - \exp(-\pi) \approx 95.7\%$, so losing most of the signal.
3. The imaginary part of $-\beta/r_0$ can be interpreted as an amplitude loss factor per unit length ($r_0\theta$ is the arc length at the waveguide centerline); noticing that, as r_0 grows, the geometry becomes closer to a straight waveguide, then $\beta/r_0 \rightarrow \sqrt{\mu_{\text{straight}}}$. For all three modes, the reader may verify the similarity between $\sqrt{\mu} = \beta/r_0$ in Tables 5, 6, 7 and the values of $\sqrt{\mu_{\text{straight}}}$ in Table 4, as well as the rapid growth of $-\operatorname{Im}(\beta)$ as the bending becomes tighter (that is, as r_0 decreases).

Numerical results using the impedance BC. In all of our numerical experiments, we use the waveguide data provided in Table 3. Using the solution (4.1) to the eigenproblem (2.3), and its accompanying numerical method for finding the unknown coefficients, we compute the eigenvalues λ for the only three propagating modes: {first even mode, first odd mode, second even mode}. In order to determine an appropriate initial guess for λ in the coiled waveguide problem, we first solve the straight waveguide problem:³

$$\begin{aligned} u'' + (k_0^2 n^2 - \mu_{\text{straight}})u &= 0, \\ \llbracket u(\pm a) \rrbracket &= 0, \quad \llbracket u'(\pm a) \rrbracket = 0, \\ u'(-b) &= 0, \quad u'(b) - idk_0 n(b)u(b) = 0. \end{aligned} \tag{4.6}$$

For both cases, $d = 0$ and $d = 1.45$, Table 4 contains the predicted values of μ_{straight} and its square root, which will be compared with β/r_0 in our forthcoming results for the circularly coiled waveguides. Notice that the difference between the results of these two cases is restricted to the imaginary part, and is many orders of magnitude smaller than their real parts. To initialize the coiled waveguide eigenproblem solver with a given r_0 , the eigenvalues μ_{straight} are multiplied by $1.0001 \cdot r_0^2$. The values of the $d = 1.45$ case are used as seeds for the present set of results (i.e.,

³Finding the eigenvalues of this straight waveguide problem requires solving transcendental equations that involve hyperbolic and trigonometric functions, which are derived so that all the interface and boundary conditions are satisfied [5].

with impedance BC), while those of $d = 0$ are utilized for the results in the next two sections (i.e., without impedance BC).

We moreover mention that these results for the straight waveguide have been obtained from a quadruple precision implementation, making little reliable any result whose real and imaginary parts differ by more than 30 orders of magnitude. However, it was observed that despite the inaccuracy of the imaginary part, the convergence in the Fortran implementation gets benefited from that non-real starting point, while the Neumann BC guess may cause a failed convergence. The Julia code, in turn, can indistinctly take advantage of both of the initial guesses (with $d = 0$ and $d = 1.45$) to converge to the same result in a similar number of Newton iterations.

Table 4: Computed eigenvalues for three propagating modes in a straight three-layer waveguide using Neumann ($d = 0$) or impedance ($d = 1.45$) BCs on the right boundary. The digits, or entire values, of the impedance BC's results that differ from the Neumann BC's are shaded.

		$d = 0$		$d = 1.45$	
Mode		μ_{straight}	$\sqrt{\mu_{\text{straight}}}$	μ_{straight}	$\sqrt{\mu_{\text{straight}}}$
1 st Even	Re	$4.73785763924115 \cdot 10^4$	$2.17666204065793 \cdot 10^2$	$4.73785763924115 \cdot 10^4$	$2.17666204065793 \cdot 10^2$
	Im	0	0	$-1.28929634312106 \cdot 10^{-34}$	$-2.9616364852197 \cdot 10^{-37}$
1 st Odd	Re	$4.73594553855486 \cdot 10^4$	$2.17622276859582 \cdot 10^2$	$4.73594553855486 \cdot 10^4$	$2.17622276859582 \cdot 10^2$
	Im	0	0	$-2.12986190583761 \cdot 10^{-29}$	$-4.89348318695304 \cdot 10^{-32}$
2 nd Even	Re	$4.73251454095355 \cdot 10^4$	$2.17543433386383 \cdot 10^2$	$4.73251454095355 \cdot 10^4$	$2.17543433386383 \cdot 10^2$
	Im	0	0	$-6.92081537949382 \cdot 10^{-20}$	$-1.59067439355929 \cdot 10^{-22}$

Using our largest bend radius, $r_0 = 13000$, the resulting mode profiles are depicted in Fig. 3 and their corresponding eigenvalues are delineated in Table 5. Because of this very weak bending, the mode profiles appear nearly identical to those of a straight waveguide, being highly symmetric/antisymmetric about the center of the waveguide. However, their eigenvalues do exhibit some minuscule losses ($\text{Im}(\beta) < 0$) induced by this slight circular coiling. According to the above suggested interpretation of the numerical results for β , at this bending curvature it may take millions of coils to get a perceivable loss in the second even mode and many more orders of magnitude to affect the amplitude of the first even and odd modes.

Table 5: Real and imaginary components of the eigenvalues of the first two even modes and the first odd mode of (2.3) at $r_0 = 13000$ using the impedance BC (4.5). See Fig. 3 for their corresponding mode profiles. When comparing the last column to the straight waveguide's eigenvalues, $\sqrt{\mu_{\text{straight}}}$ (see Table 4), note that the leading figures of the real part remain equal, but the imaginary parts are some orders of magnitude larger (the digits that differ are shaded).

$r_0 = 13000$		λ	$\beta = \sqrt{\lambda}$	$\beta/r_0 = \sqrt{\mu}$
1 st even mode	Re	$8.00620263404956 \cdot 10^{12}$	$2.82952339344448 \cdot 10^6$	$2.17655645649575 \cdot 10^2$
	Im	$-2.623592454862567 \cdot 10^{-21}$	$-4.636103134791148 \cdot 10^{-28}$	$-3.566233180608575 \cdot 10^{-32}$
1 st odd mode	Re	$8.00294378462047 \cdot 10^{12}$	$2.82894746939926 \cdot 10^6$	$2.17611343799943 \cdot 10^2$
	Im	$-4.15317011697652 \cdot 10^{-15}$	$-7.34048645636122 \cdot 10^{-22}$	$-5.64652804335478 \cdot 10^{-26}$
2 nd even mode	Re	$7.99795845391453 \cdot 10^{12}$	$2.82806620394830 \cdot 10^6$	$2.17543554149869 \cdot 10^2$
	Im	-2.21912100071211	$-3.92338941290335 \cdot 10^{-7}$	$-3.01799185607950 \cdot 10^{-11}$

Focusing on the second even mode, which is more susceptible to the coiling effect, and tightening

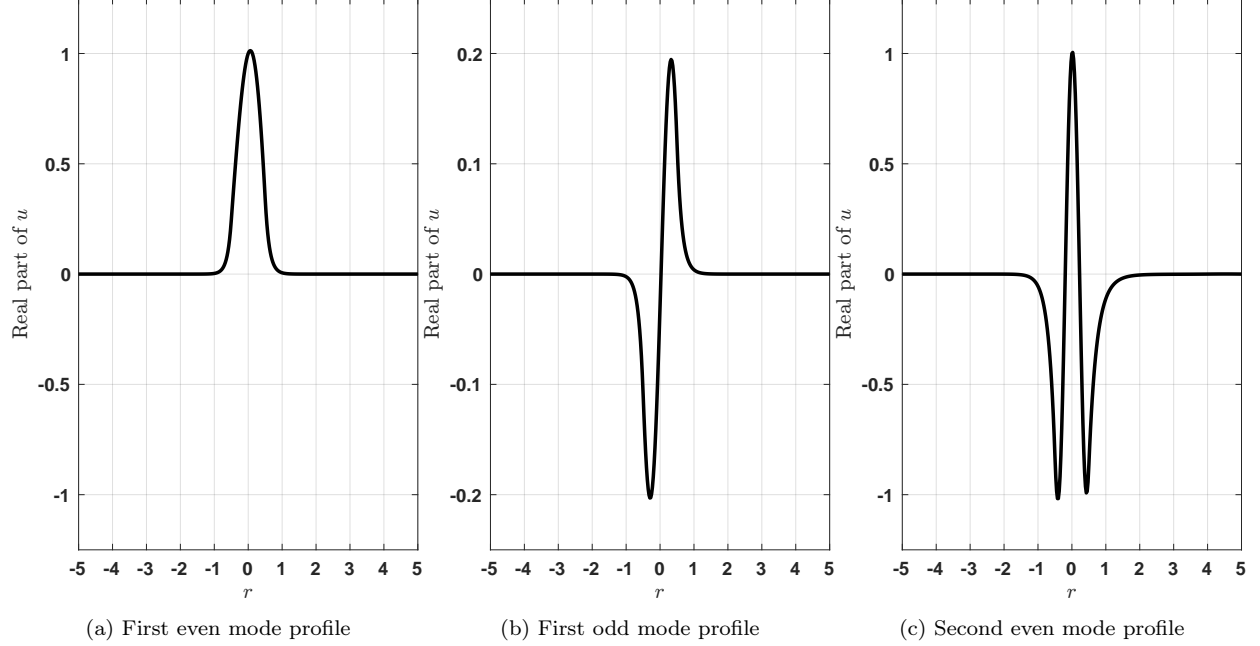


Figure 3: Real components of the mode profiles of the three-layer waveguide (2.3) at $r_0 = 13000$ with impedance BC (4.5), which are nearly indistinguishable from the straight waveguide case. Notice that the coordinate r has been re-centered at zero. See Table 5 for their corresponding eigenvalues.

the bend radius (r_0), one first sees some oscillations on the outside of the bend, which grow in magnitude as the coil radius is decreased (see Fig. 4). The results listed in Table 6 show that the predicted eigenvalues are becoming more lossy as the bend radius decreases; this result is expected since the bending reduces the waveguide's ability to entirely guide the modes. Rather, some mode energy leaks out and the mode develops a confinement loss. Compare these results with those of the model's predicted solutions when using a PML BC, found in Fig. 6 and Table 7.

Table 6: Model estimated eigenvalues, using the impedance BC (4.5), of the second even mode as the coiling radius is tightened. Figure 4 illustrates their corresponding mode profiles. Compare these model predicted mode eigenvalues with those delineated in Table 7, which were computed using a PML BC; the digits, or entire values, that differ are shaded.

r_0		λ	$\beta = \sqrt{\lambda}$	$\beta/r_0 = \sqrt{\mu}$
10400	Re	5.11869686714306 $\cdot 10^{12}$	2.26245372707224 $\cdot 10^6$	2.17543627603100 $\cdot 10^2$
	Im	-1.21328979840387 $\cdot 10^2$	-2.68135826135536 $\cdot 10^{-5}$	-2.57822909745708 $\cdot 10^{-9}$
7800	Re	2.87927157786418 $\cdot 10^{12}$	1.69684164784584 $\cdot 10^6$	2.17543801005877 $\cdot 10^2$
	Im	-5.76638397398440 $\cdot 10^3$	-1.69915206327735 $\cdot 10^{-3}$	-2.17840008112481 $\cdot 10^{-7}$
5200	Re	1.27962392974873 $\cdot 10^{12}$	1.13120463654890 $\cdot 10^6$	2.17539353182480 $\cdot 10^2$
	Im	-2.25075256570834 $\cdot 10^6$	-0.994847657526836	-1.91316857216699 $\cdot 10^{-4}$

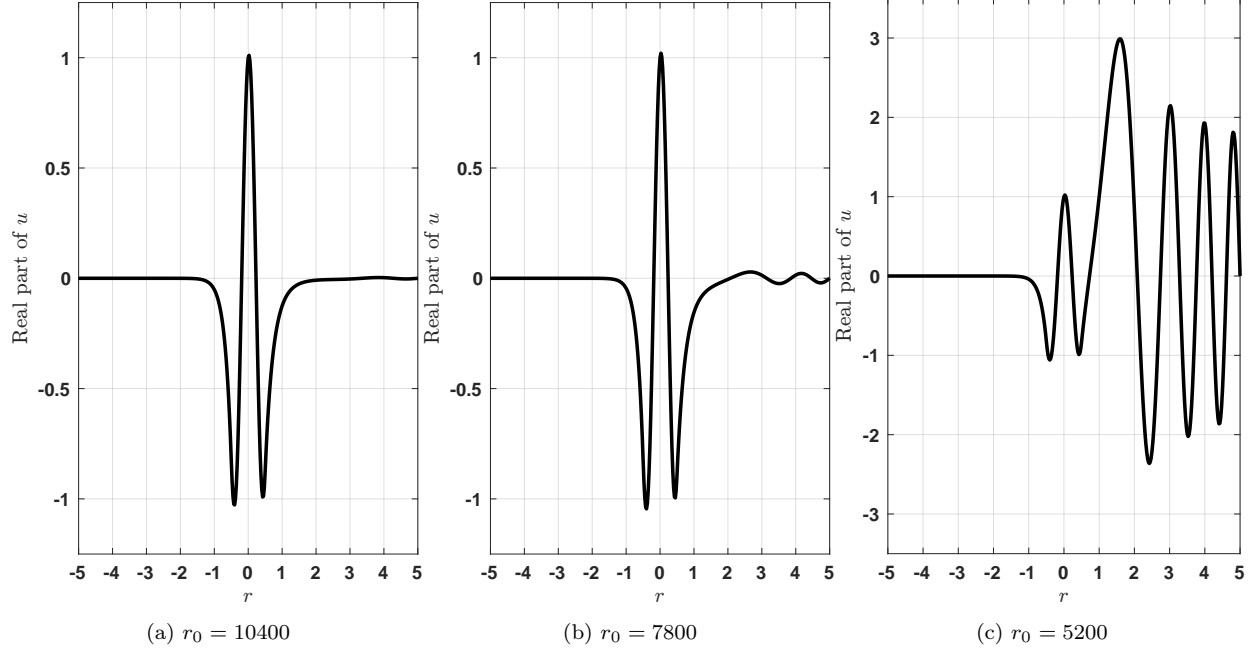


Figure 4: Real component of the second even mode's profile in the three-layer bent waveguide when using the impedance BC (4.5), for three distinct bend radii r_0 . Examine the data in Table 6 for their corresponding eigenvalue information. Compare these mode profiles with those portrayed in Fig. 6, which are computed using a PML BC.

5 Replacing the impedance BC with a perfectly matched layer

It is well known that the impedance BC is a good approximation of the radiation condition provided that the outgoing wave is exiting mostly in the normal direction to the surface of the boundary. For the three-layer circularly coiled waveguide problem, the wave predominantly exits in the tangential direction, so the impedance BC's validity for approximating a proper radiation condition (as in an open waveguide) is at best questionable. Presently, we will demonstrate that the impedance BC can be replaced with a much more accurate *perfectly matched layer* (PML).

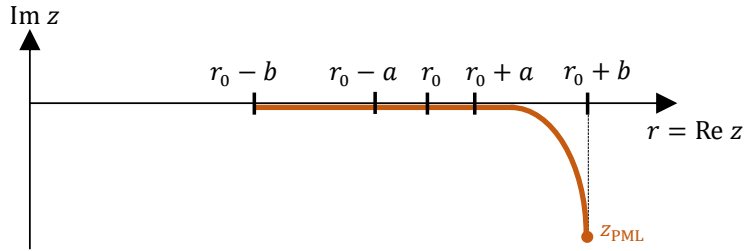


Figure 5: Passing from a segment in the real line to a path in the complex plane, inspired by the PML methodology. The goal of extending the solution to the complex plane is to capture the decay that the outgoing wave function is expected to present when evaluated on the (orange) curved path. Such decaying behavior is enforced through the constraint $u = 0$ at $z = z_{\text{PML}}$.

The construction of a PML BC can be accomplished in a few steps and is supported by the following arguments:

- The solution is holomorphic in r and thus admits a holomorphic extension. In simple words, it is allowed to replace the independent real-valued variable r with a complex-valued argument z , so that the derivatives in the original Bessel equation (1.3) are then understood in the complex sense.
- The original solution has been traced along $r = \text{Re}(z)$. This makes differentiating between the outgoing and incoming waves impossible, until the imaginary component of z is re-introduced. Therefore, by having z dive into the complex plane in a layer near the boundary (PML), as is depicted in Fig. 5, we are able to distinguish ingoing and outgoing waves, thanks to the mathematical argumentation outlined next.
- Marcuse [17, pp. 408] shows that the outgoing solution in the outer cladding is a Hankel function of the second kind, of order β , with an argument scaled by $k_0 n_{\text{clad}}$, i.e., $H_{\beta}^{(2)}(k_0 n_{\text{clad}} z)$. According to the asymptotic properties of these Hankel functions (see [22, §10.2, §10.7] or [8, §8.451]), we have

$$H_{\beta}^{(2)}(k_0 n_{\text{clad}} z) \approx \sqrt{\frac{2}{\pi k_0 n_{\text{clad}} z}} \exp\{-i(k_0 n_{\text{clad}} z - \beta\pi/2 - \pi/4)\} \quad (5.1)$$

with the truncation error, in *little-o* notation, being estimated by $o(|\text{Im}(k_0 n_{\text{clad}} z)|)$ as $z \rightarrow \infty$. The asymptotic expression for the corresponding Hankel function of the first kind, $H_{\beta}^{(1)}$, which models an incoming wave at the boundary, differs only by the leading sign in the exponential. By tracing the solution of our Bessel equation along a path where z has an increasingly negative imaginary part, outgoing waves (i.e., $H_{\beta}^{(2)}$ functions) decay exponentially, whereas incoming waves (i.e., $H_{\beta}^{(1)}$ functions) grow exponentially.

- In order to implement the PML in practice, we designate the new path in the boundary layer by the formula $z = z(r)$, and appropriately modify the governing relation (1.3). It is important to realize that the projection of the solution onto power series expansions remains valid even after implementing the complex argument z in the boundary layer (see Remark 3 about the additional coordinate transformation applied to x). The new complex-valued path $z(r)$ needs to start at a point on the real line between $r_0 + a$ and $r_0 + b$ and to converge smoothly to a preset point z_{PML} (see Fig. 5), which has a negative imaginary part that depends on the cladding wavenumber κ_1 and a positive real parameter C_{PML} , which controls the strength of the PML absorption:

$$z_{\text{PML}} = r_0 + b - i \frac{C_{\text{PML}}}{\kappa_1}, \quad (5.2)$$

In the PML literature, the path toward the point (5.2) is usually a polynomial curve. At the end of this layer (at $r = r_0 + b$), the impedance BC is replaced with a zero-valued Dirichlet BC for the modified governing equation (in terms of z):

$$u(z_{\text{PML}}) = 0. \quad (5.3)$$

The Dirichlet BC enforced at $z = z_{\text{PML}}$ eliminates incoming waves while leaving outgoing waves unaffected (up to machine precision), because, at that point, the latter are mostly

attenuated/absorbed. Moreover, the choice of a particular path through the PML does not matter because the Dirichlet BC is enforced only at the final point and the algorithm never evaluates the power series at other points along the path, and makes no use of the particular curve parameterization (e.g., derivatives with respect to z are not required for computations). Finally, notice that replacing the impedance BC with (5.3) significantly simplifies the non-linear eigensolve process and it enforces the correct radiation condition, leading to far more trustworthy solutions to our bent waveguide problem.

- More information on the implementation of a PML for solving PDEs numerically is found in Bérenger’s publication [1] for finite difference methods and in [4, 18, 24] for finite element methods.

REMARK 2 As presented in [4], Collino and Monk carried out the impact analysis on the Hankel function’s asymptotic behavior (5.1). In their case, however, they used the $H_\beta^{(1)}$ Hankel functions rather than $H_\beta^{(2)}$, as well as a PML path with positive imaginary components due to their choice of sign (convention) in the time-harmonic ansatz (which is opposite to the one used in the present work, that coincides with the ansatz in [17]). ■

REMARK 3 It is important to emphasize that $z = z_{\text{PML}}$ replaces the physical coordinate $r = r_0 + b$, and not the transformed coordinate $x_2 = b_2$ defined in (4.1). Only after transforming $r \mapsto z(r)$ in the PML region, is the transformation made to x_2 :

$$x_2 \leftarrow (r_0 + a) \ln \left(\frac{z(r)}{r_0 + a} \right).$$

Thus, the evaluation of the power series at the end of the right cladding region (with argument x_2) must be evaluated at

$$b_2 \leftarrow b_{2,\text{PML}} = (r_0 + a) \ln \left(\frac{z_{\text{PML}}}{r_0 + a} \right).$$

The complex-valued natural logarithm is evaluated in its principal branch so that its imaginary part is in the interval $[-\pi, \pi)$. ■

Numerical experiments using the PML BC. Using the same conditions and waveguide properties as were utilized in Section 4, the eigensolutions are computed using the PML BC (5.3), rather than the impedance BC, as the bend radius is varied. We set the end of the boundary layer to be the point z_{PML} defined by (5.2), using a PML strength of $C_{\text{PML}} = 800$. For completeness, we mention that the PML path is assumed to begin at the midpoint between the core-cladding interface and the right boundary; that choice, however, does not impact the eigenvalue solver, and is not relevant to this section’s graphs because the mode profile plots are traced along the real axis.

Fig. 6 displays the predicted second even mode profiles under three distinct bend radii; the corresponding eigenvalue results are tabulated in Table 7. Note the differences in the outgoing oscillations’ period and amplitude observed in the predicted mode profile (particularly big in the

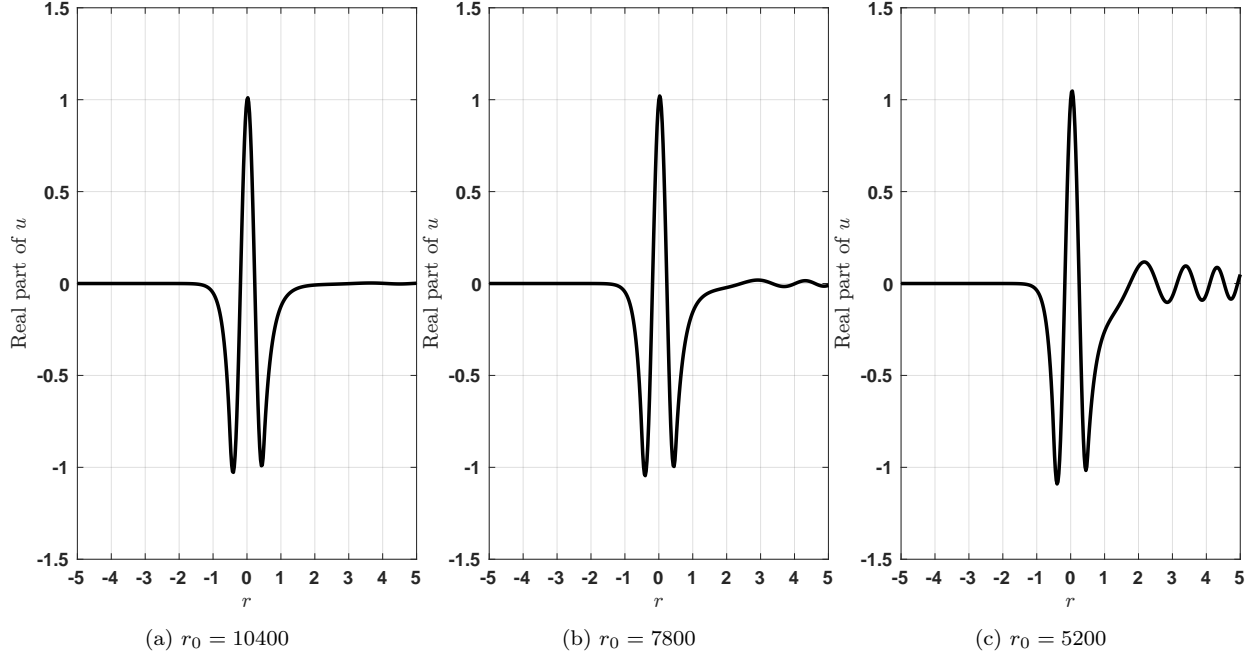


Figure 6: Predicted real component of the second even mode's profile in the three-layer coiled waveguide using a PML BC for different bend radii. The corresponding eigenvalue information is listed in Table 7. Compare these mode profiles with those shown in Fig. 4, which are computed using an impedance BC, to observe the differences in the features of the radiating oscillations toward the right boundary of the waveguide.

$r_0 = 5200$ case), when using the PML BC (Fig. 6) in comparison with the one with the impedance BC (Fig. 4), even though the computed eigenvalues are still quite similar to one another (all of the imaginary components are surprisingly on the same order of magnitude, cf. Table 6 vs. Table 7).

We continue the comparison of the results obtained with both BC settings by observing the propagation constant, β , of all the propagating modes at different bend radii. Moreover, we add a smaller value for r_0 , which does not lead to a successful convergence with the impedance BC but it does deliver a satisfactory result under the PML approach. Table 8 contains all the resulting values of β , comparing the the impedance BC and the PML approach, for the two even modes and the odd mode and four bend radii. What is remarkable in the results on Table 8 is that the real part of β practically varies linearly with r_0 , but the imaginary part grows (in absolute value) close

Table 7: Computed eigenvalues, using a PML BC, of the second even mode as the coiling radius is tightened. Figure 6 depicts their corresponding mode profiles. Compare these model-predicted mode eigenvalues with those delineated in Table 6, which were computed using an impedance BC: the digits, or entire values, that differ are shaded.

r_0		λ	$\beta = \sqrt{\lambda}$	$\sqrt{\mu} = \beta/r_0$
10400	Re	5.11869686447172 $\cdot 10^{12}$	2.26245372648187 $\cdot 10^6$	2.17543627546334 $\cdot 10^2$
	Im	-3.59916299495178 $\cdot 10^3$	-7.95411405065176 $\cdot 10^{-4}$	-7.64818658716516 $\cdot 10^{-8}$
7800	Re	2.87927168048203 $\cdot 10^{12}$	1.69684167808374 $\cdot 10^6$	2.1754380488253076 $\cdot 10^2$
	Im	-1.00373251044341 $\cdot 10^5$	-0.0295764927101785	-3.79185803976647 $\cdot 10^{-6}$
5200	Re	1.27968375031025 $\cdot 10^{12}$	1.13123107732720 $\cdot 10^6$	2.17544437947539 $\cdot 10^2$
	Im	-1.76816227029980 $\cdot 10^6$	-0.781521258449466	-1.5029254970182 $\cdot 10^{-4}$

to exponentially as r_0 decreases. Apart from that observation, an important takeaway is that at the smallest r_0 the value of $-\text{Im}(\beta)$ of the second even mode induces a 99.99% loss in about one radian. The odd mode, in turn, requires a few dozen coils to fully vanish. The first mode, however, even at the tightest bend, exhibits a loss factor that needs to act for nearly a million coils to make it vanish.

Table 8: Comparison of the model predicted mode propagation constants in the three-layer circularly bent waveguide for three distinct bend radii, using either the impedance BC or the PML BC, applied at $r = r_0 + b$. The digits, or entire values, that differ between the two conditions are shaded in the impedance BC column only. The real components tend to be more aligned than the imaginary components, and, at least for this specific problem, are of the same order of magnitude. Moreover, the imaginary components are better matched between these two BCs for weaker bends (i.e. larger bend radii). Because the PML BC is a better representation of the proper radiation condition, its results are trusted to be more accurate than those found using the impedance BC.

Mode	r_0		β (using impedance BC)	β (using PML BC)
1 st Even	10400	Re	$2.26362060047958 \cdot 10^6$	$2.26362060047958 \cdot 10^6$
		Im	$-1.02194399501288 \cdot 10^{-26}$	$-2.63161591219032 \cdot 10^{-30}$
1 st Even	7800	Re	$1.69771848771636 \cdot 10^6$	$1.69771848771636 \cdot 10^6$
		Im	$-3.55201875479254 \cdot 10^{-24}$	$-7.37577942903455 \cdot 10^{-25}$
1 st Even	5200	Re	$1.13184377894959 \cdot 10^6$	$1.13181802321074 \cdot 10^6$
		Im	-1.00005695603398	$-2.04607567975992 \cdot 10^{-15}$
1 st Even	2600	Re	N.A.	$5.65923463817321 \cdot 10^5$
		Im	N.A.	$-3.21177027104337 \cdot 10^{-6}$
1 st Odd	10400	Re	$2.26315767840190 \cdot 10^6$	$2.26315767840190 \cdot 10^6$
		Im	$-4.92656786477296 \cdot 10^{-20}$	$-5.66184601060354 \cdot 10^{-20}$
1 st Odd	7800	Re	$1.69736779822896 \cdot 10^6$	$1.69736779822896 \cdot 10^6$
		Im	$-8.02404417111743 \cdot 10^{-16}$	$-4.97996447610167 \cdot 10^{-14}$
1 st Odd	5200	Re	$1.13157775618699 \cdot 10^6$	$1.13157775618741 \cdot 10^6$
		Im	$-1.51030428594905 \cdot 10^{-7}$	$-3.72804455077520 \cdot 10^{-8}$
1 st Odd	2600	Re	N.A.	$5.65787956064918 \cdot 10^5$
		Im	N.A.	-0.0159239556531208
2 nd Even	10400	Re	$2.26245372707224 \cdot 10^6$	$2.26245372648187 \cdot 10^6$
		Im	$-2.68135826135536 \cdot 10^{-5}$	$-7.95411405065176 \cdot 10^{-4}$
2 nd Even	7800	Re	$1.69684164784584 \cdot 10^6$	$1.69684167808374 \cdot 10^6$
		Im	$-1.69915206327735 \cdot 10^{-3}$	-0.0295764927101785
2 nd Even	5200	Re	$1.13120463654890 \cdot 10^6$	$1.13123107732720 \cdot 10^6$
		Im	-0.994847657526836	-0.781521258449466
2 nd Even	2600	Re	N.A.	$5.65620469836942 \cdot 10^5$
		Im	N.A.	-8.96795892357474

Unlike with larger values of r_0 , at the tightest bend corresponding to $r_0 = 2600$, it is possible to clearly visualize the coiling-induced distortion of the mode profile “leaning” toward the outside of the bend in all three modes (see Fig. 7). Looking at the location of the peak of even mode’s graph (Fig. 7a), one can ascertain that the mode is leaning to the right, as expected. Furthermore, the odd mode’s profile (Fig. 7b) exhibits visible fluctuations toward the outer boundary—an indication that the mode is leaking energy and may no longer be normalizable because the bending transformed it from a perfectly guided mode into a *leaky mode*. Finally, the second even mode at $r_0 = 2600$ (Fig. 7c)

continues the trend of increasingly stronger outgoing oscillations already seen with $r_0 = 10400$, 7800, and 5200 (in Fig. 6a, b and c, respectively), now with a noticeably higher amplitude and frequency.

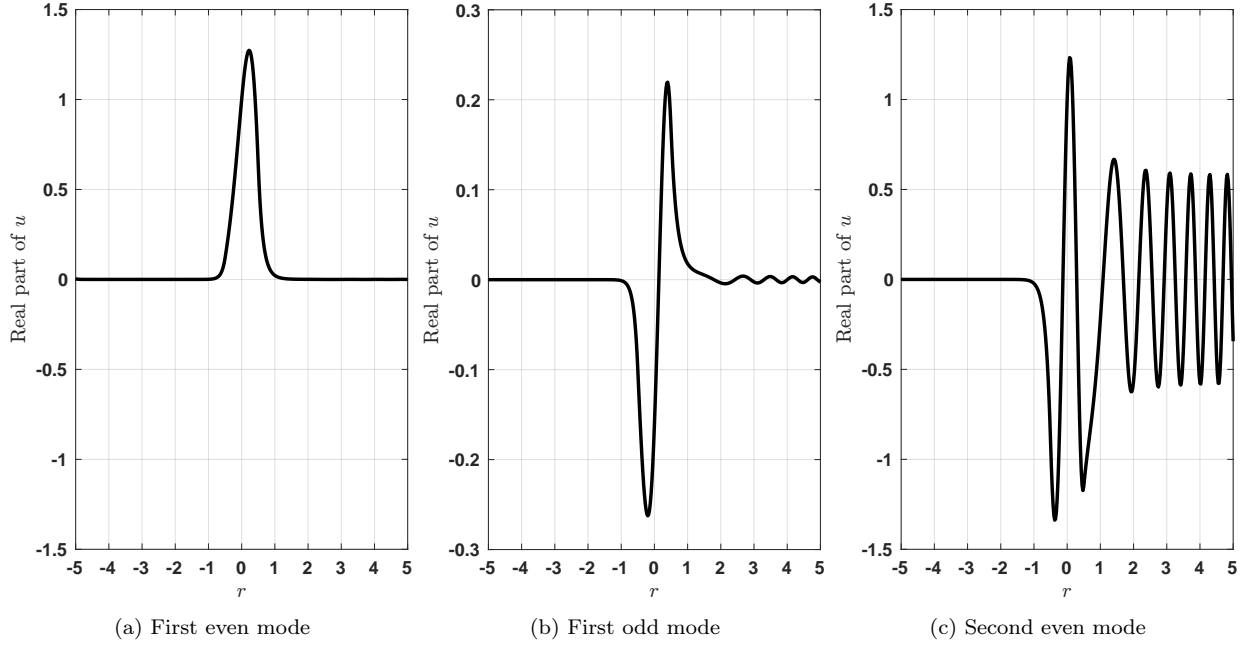


Figure 7: Predicted mode profiles of the three-layer bent waveguide using the PML BC and a bend radius of $r_0 = 2600$. All modes exhibit noticeable distortion effects from the circular coiling.

Main differences between the results with the impedance BC and the PML BC. A central takeaway of the results presented to this point is that the impedance BC provides significantly different results with respect to the ones obtained with the PML. We have already mentioned the fact that the impedance BC may be inappropriate whenever the direction of the wave incidence to the boundary is far from normal. Now, by bringing our attention to the following points evidenced in the numerical results, which remain true for both of our implementations, we gain additional insights to consider the PML BC as a plausably more accurate and trustworthy approach.

1. Note the major visual difference for the second even mode profile between the plot of Fig. 4c and the plot of Fig. 6c. Firstly, the result with the impedance BC abruptly increases (with respect to the behavior seen in Figures 6a and 6b) the amplitude of the oscillations present in the right cladding. On the contrary, the corresponding PML result displays a coherent transition between the profile at $r_0 = 7800$ (Fig. 6b) and the profile at $r_0 = 2600$ (Fig. 7c).
2. Again, by looking at Figure 4, we notice that the solution profile, after a few fluctuations, nearly vanishes at the right boundary. This responds to a magnitude disparity between the terms of the impedance BC (cf. (1.6), where the coefficient that multiplies u is much larger than the one acting on $\partial u / \partial r$). In contrast, the mode profiles obtained with the PML BC do not present that feature (consider Fig. 6 and Fig. 7).

3. In Table 8, we can observe how $\text{Im}(\beta)$ varies as r_0 decreases, and that the range of orders of magnitude through which it transits depends on the mode. Notice that, for the first even mode, $\text{Im}(\beta)$ has values in the 10^{-30} to 10^{-20} range for the two largest bend radii but, in the impedance BC case, at $r_0 = 5200$ we get a value completely out of trend ($\sim 10^0$), whereas the PML result at $r_0 = 5200$ show a good alignment with the former values, and this result is accompanied by the one at $r_0 = 2600$, which also confirms the pattern.
4. The fact that the formulation with the PML, in general, converges easier to the sought unknowns than the impedance BC case, even for smaller bend radius, supports the idea of the PML's complex-path tracing being a more appropriate or natural approximation to the outgoing radiation phenomenon.

Robustness of the predicted solution with respect to the PML parameters. We additionally study the effect of changing the parameters of the PML BC (i.e., the location of z_{PML} in both directions of the complex plane) on the computed propagation constant β . To this end, we fix the bend radius at $r_0 = 5200$ and, again focusing on the second even mode, assess how the mode's propagation constant changes as a function of the PML strength C_{PML} and the size of the layer (by modifying the real part of z_{PML}). The results of this study are listed in Table 9 for a fixed layer length and seven values of C_{PML} , and in Table 10 for a fixed PML strength parameter and four different layer lengths. These results show that the predicted eigenvalue behaves robustly with regard to the PML parameters, since its value has quite small variations over a wide range of the PML parameters. While it is much less sensitive to the size of the PML, it does require a sufficiently large PML strength parameter, C_{PML} , to become steady. However, if C_{PML} grows too much, the computations are somewhat slower. On the other hand, even though several of the PML lengths return the same 15 digits of β , for the sake of simplicity and symmetry, using the original z_{PML} defined in (5.2) is recommended. Consequently, we consider the case with $C_{\text{PML}} = 800$ and $z_{\text{PML}} = r_0 + b - i C_{\text{PML}}/\kappa_1$ (see fifth row of Table 9 and first row of Table 10, respectively) as the reference solution against which the remaining results are compared, particularly because $C_{\text{PML}} = 800$ is the smallest value at which the first fifteen digits in both $\text{Re}(\beta)$ and $\text{Im}(\beta)$ get fixed, without causing a noticeably lower computational speed.

6 Comparison with loss formulas for the bent slab waveguide

Finally, we compare our results with values obtained from mode bend loss formulas that are available in the literature; these algebraic formulas provide the loss factor per radian, corresponding to the $-\text{Im}(\beta)$ values in our notation. The comparison includes results from three sources relevant to our methodology [14, 17, 27]; all three contributions account only for geometric effects and provide closed formulas that are easy to implement.

The earliest of these results is the one by Marcatili [14]. This work covers circular waveguides with a rectangular cross-section and with the possibility of four different refractive indices

Table 9: Predicted eigenvalues of the second even mode for a fixed bend radius of $r_0 = 5200$, using the PML BC applied at $z_{\text{PML}} = r_0 + b - i C_{\text{PML}}/\kappa_1$, as a function of the parameter C_{PML} . We highlight in gray all the digits that differ from the reference solution: $C_{\text{PML}} = 800$ case. The computational speed noticeably decreased as C_{PML} increased, especially for the $C_{\text{PML}} = 1600$ and $C_{\text{PML}} = 3200$ cases.

$r_0 = 5200$		β Using the PML BC
$C_{\text{PML}} = 50$	Re	0.113123111157010 $\cdot 10^7$
	Im	-0.765959119625596
$C_{\text{PML}} = 100$	Re	0.113123107805648 $\cdot 10^7$
	Im	-0.781048100766258
$C_{\text{PML}} = 200$	Re	0.113123107732733 $\cdot 10^7$
	Im	-0.781520834783452
$C_{\text{PML}} = 400$	Re	0.113123107732720 $\cdot 10^7$
	Im	-0.781521258449540
$C_{\text{PML}} = 800$	Re	0.113123107732720 $\cdot 10^7$
	Im	-0.781521258449466
$C_{\text{PML}} = 1600$	Re	0.113123107732720 $\cdot 10^7$
	Im	-0.781521258449466
$C_{\text{PML}} = 3200$	Re	0.113123107732720 $\cdot 10^7$
	Im	-0.781521258449466

Table 10: Computed eigenvalues of the second even mode for a fixed bend radius, $r_0 = 5200$, and PML strength, $C_{\text{PML}} = 800$, using a PML BC with the boundary layers ending at different locations of z_{PML} . All of the digits that differ from the reference solution (first row) are highlighted in gray.

$r_0 = 5200, C_{\text{PML}} = 800$		β Using the PML BC
$z_{\text{PML}} = r_0 + b - i C_{\text{PML}}/\kappa_1$	Re	0.113123107732720 $\cdot 10^7$
	Im	-0.781521258449466
$z_{\text{PML}} = r_0 + a + 0.75(b-a) - i C_{\text{PML}}/\kappa_1$	Re	0.113123107732720 $\cdot 10^7$
	Im	-0.781521258449466
$z_{\text{PML}} = r_0 + a + 0.50(b-a) - i C_{\text{PML}}/\kappa_1$	Re	0.113123107732720 $\cdot 10^7$
	Im	-0.781521258449466
$z_{\text{PML}} = r_0 + a + 0.25(b-a) - i C_{\text{PML}}/\kappa_1$	Re	0.113123107732720 $\cdot 10^7$
	Im	-0.781521258449455

in its subdomains. The slab problem reduces to a particular scenario where only two indices are needed. The methodology for obtaining Marcatili's loss formula consists of solving an approximate complex-valued eigenvalue equation, making an extensive exploitation of Hankel and Bessel function properties, along with approximations based on the bending ratio and the ratio of the refractive indices. The formula is ultimately applicable only to the fundamental transverse mode of the waveguide, but with two different polarization directions. We use the formula (19) of [14], which best coincides with our problem setup.

For the second reference, we rely on the classic book by Marcuse [17]. His loss estimation avoids the search for a complex-valued eigenvalue and instead applies the "approximation by tangents" expressions for the Hankel functions, available in [8, p. 8.452], as well as other algebraic manipulations and the asymptotic approximation found in (5.1). The resulting formula, (9.6-27) in the book,

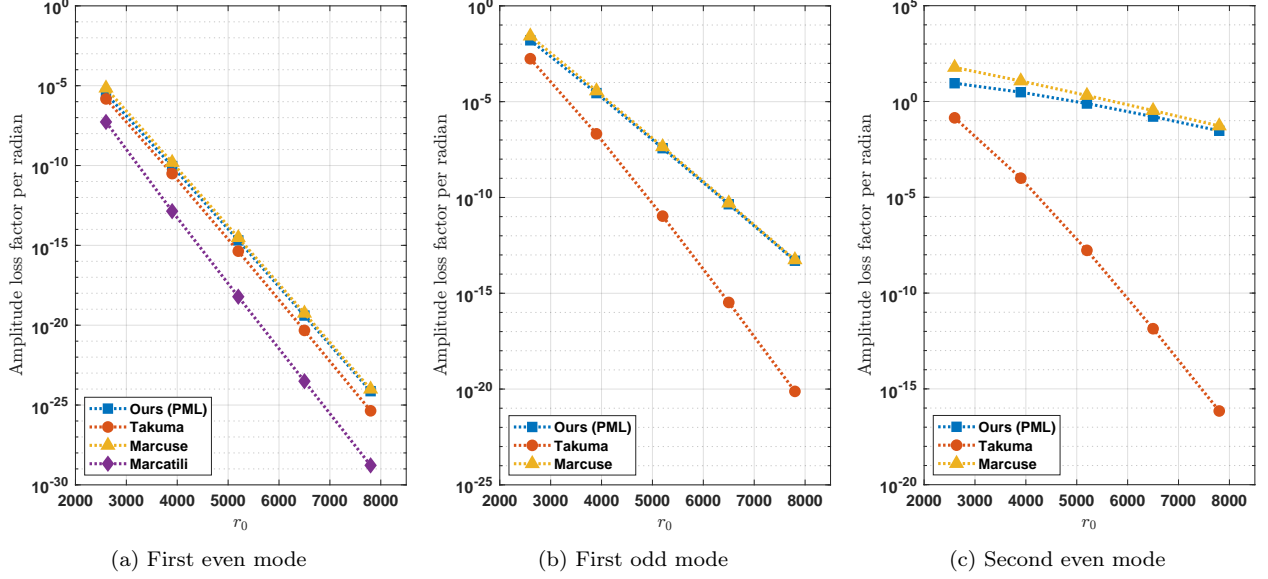


Figure 8: Comparison of the circularly curved three-layer waveguide’s amplitude loss factors, $-\text{Im}(\beta)$, as a function of the bend radius (r_0) for the (a) first even mode, (b) first odd mode, and (c) second even mode. Results obtained with our numerical approach using the PML BC are compared with loss values obtained with formulas from the literature by Marcatili [14], Marcuse [17], and Takuma et al. [27].

can be applied to any mode as long as we know the real propagation constants of the straight slab waveguide’s modes.

The third reference is from the work by Takuma et al. [27]. Their work is based on a change of variables and a truncated series in terms of the bending radius, in combination with the solutions to the straight slab waveguide’s eigenvalue equation and several approximations and corrections. Their formula, equation (43) of [27], is applicable to any mode, $n = 0, 1, 2, \dots$, but the authors acknowledge the inaccuracy of their approach to correctly capture the propagation constant (eigenvalue) in higher-order modes ($n \geq 1$).

We compute the mode bend loss estimates from these three formulas and compare them with the values computed with our methodology for the first three modes of the waveguide using five different bend radii, between 2600 and 7800. Fig. 8 depicts the results of this comparison; note that we show results from Marcatili’s formula only for the fundamental mode (i.e., the first even mode) where this formula is applicable (Fig. 8a). We observe that in all cases, Marcuse’s formula remains close to our results throughout the entire range of bend radii, always matching to at least the same order of magnitude. Marcatili’s formula is the farthest for the first even mode, while Takuma’s formula is within one order of magnitude only for this fundamental mode and strongly diverges from our results for the other two modes.

As expected, the losses decrease as the bend radius increases, and the higher-order modes (i.e., the first odd mode and the second even mode) exhibit higher rates of loss than the fundamental mode. The effect of higher-order modes having higher bend losses than their lower-order mode counterparts is called *differential mode loss* [25, §5C], and is often used to filter out unwanted higher-order modes from the waveguide output.

7 Conclusions

We have presented a study of circularly coiled waveguides with data well-matched to standard step-index optical fibers. This results in an eigenproblem with complex-valued eigenvalues that are embedded into the orders of their corresponding eigenvectors, which consists of Bessel functions. And, these eigensolutions also have large (in magnitude) complex-valued arguments. Such Bessel functions are difficult to reliably and accurately evaluate numerically. We demonstrated that, by applying a conformal mapping (2.2) on the independent variable, and using the Frobenius method, we can produce a recursion relation that is beneficial for computing these Bessel functions with large arguments and complex-valued orders; by using high-precision floating-point arithmetic in our implementations, we ensured accurate results. Furthermore, we presented a methodology for evaluating the eigenfunctions for the bent waveguide problem by leveraging the known analytical solutions to its analogous straight waveguide configuration as initial conditions in the numerical solver. Most importantly, we were able to replace the traditionally used impedance BC along the outside of the bend in the fiber with a PML that appears to be more reliable and robust for imposing the radiation condition in the eigenvalue problem. Our numerical experiments show that this PML BC produces results that can be orders of magnitude different than those that are found with the impedance BC, especially in the imaginary component of the eigenvalue (which is tied to the confinement loss of the mode) and for cases of tighter bend radii (i.e. smaller values of the bend radius r_0). In future work, we intend to use the improved accuracy of these first few eigenmode solutions to the coiled slab waveguide for verifying and benchmarking the numerical solutions of our 3D Maxwell finite element model of the bent slab waveguide.

References

- [1] J.-P. Bérenger. “A perfectly matched layer for the absorption of electromagnetic waves”. In: *Journal of Computational Physics* 114.2 (1994), pp. 185–200. DOI: [10.1006/jcph.1994.1159](https://doi.org/10.1006/jcph.1994.1159).
- [2] J. Bezanson, A. Edelman, S. Karpinski, and V. B. Shah. “Julia: A fresh approach to numerical computing”. In: *SIAM Review* 59.1 (2017), pp. 65–98. DOI: [10.1137/141000671](https://doi.org/10.1137/141000671).
- [3] C. D. Butter and G. B. Hocker. “Fiber optics strain gauge”. In: *Applied Optics* 17.18 (1978), pp. 2867–2869. DOI: [10.1364/AO.17.002867](https://doi.org/10.1364/AO.17.002867).
- [4] F. Collino and P. Monk. “The perfectly matched layer in curvilinear coordinates”. In: *SIAM Journal on Scientific Computing* 19.6 (1998), pp. 2061–2090. DOI: [10.1137/S1064827596301406](https://doi.org/10.1137/S1064827596301406).
- [5] L. Demkowicz, J. Gopalakrishnan, and N. Heuer. “Stability analysis for acoustic waveguides. Part 3: Impedance boundary conditions”. In: *Applications of Mathematics* (2024). DOI: [10.21136/AM.2024.0080-24](https://doi.org/10.21136/AM.2024.0080-24).
- [6] L. Faustini and G. Martini. “Bend loss in single-mode fibers”. In: *Journal of Lightwave Technology* 15.4 (1997), pp. 671–679. DOI: [10.1109/50.566689](https://doi.org/10.1109/50.566689).
- [7] I. Gohberg and M. Krein. *Introduction to the Theory of Linear Nonselfadjoint Operators in Hilbert Space*. Providence: American Mathematical Society, 1965. ISBN: 9780821886502.

- [8] I. S. Gradshteyn and I. M. Ryzhik. *Table of integrals, series, and products*. Academic press, 2014. DOI: [10.1016/C2010-0-64839-5](https://doi.org/10.1016/C2010-0-64839-5).
- [9] M. Heiblum and J. Harris. “Analysis of curved optical waveguides by conformal transformation”. In: *IEEE Journal of Quantum Electronics* 11.2 (1975), pp. 75–83. DOI: [10.1109/JQE.1975.1068563](https://doi.org/10.1109/JQE.1975.1068563).
- [10] S. Henneking, J. Grosek, and L. Demkowicz. “A vectorial envelope Maxwell formulation for electromagnetic waveguides with application to nonlinear fiber optics”. In: *Computers & Mathematics with Applications* 193 (2025), pp. 34–53. DOI: [10.1016/j.camwa.2025.05.026](https://doi.org/10.1016/j.camwa.2025.05.026).
- [11] S. Henneking, J. Grosek, and L. Demkowicz. “Model and computational advancements to full vectorial Maxwell model for studying fiber amplifiers”. In: *Computers & Mathematics with Applications* 85 (2021), pp. 30–41. DOI: [10.1016/j.camwa.2021.01.006](https://doi.org/10.1016/j.camwa.2021.01.006).
- [12] S. Henneking, J. Grosek, and L. Demkowicz. “Parallel simulations of high-power optical fiber amplifiers”. In: *Spectral and High Order Methods for Partial Differential Equations ICOSA-HOM 2020+1*. Ed. by J. M. Melenk, I. Perugia, J. Schöberl, and C. Schwab. Springer, 2022, pp. 349–360. DOI: [10.1007/978-3-031-20432-6](https://doi.org/10.1007/978-3-031-20432-6).
- [13] S. Henneking et al. “hp3D: A scalable MPI/OpenMP hp-adaptive finite element software library for complex multiphysics applications”. In: *Journal of Open Source Software* 9.95 (2024), p. 5946. DOI: [10.21105/joss.05946](https://doi.org/10.21105/joss.05946).
- [14] E. A. J. Marcatili. “Bends in optical dielectric guides”. In: *Bell System Technical Journal* 48.7 (1969), pp. 2103–2132. DOI: [10.1002/j.1538-7305.1969.tb01167.x](https://doi.org/10.1002/j.1538-7305.1969.tb01167.x).
- [15] D. Marcuse. “Curvature loss formula for optical fibers”. In: *Journal of the Optical Society of America* 66.3 (1976), pp. 216–220. DOI: [10.1364/JOSA.66.000216](https://doi.org/10.1364/JOSA.66.000216).
- [16] D. Marcuse. “Influence of curvature on the losses of doubly clad fibers”. In: *Applied Optics* 21.23 (1982), pp. 4208–4213. DOI: [10.1364/AO.21.004208](https://doi.org/10.1364/AO.21.004208).
- [17] D. Marcuse. *Light transmission optics*. Second. Van Nostrand Reinhold, 1982. ISBN: 978-0442263096.
- [18] P. Matuszyk and L. Demkowicz. “Parametric finite elements, exact sequences and perfectly matched layers”. In: *Computational Mechanics* 51.1 (2013), pp. 35–45. DOI: [10.1007/s00466-012-0702-1](https://doi.org/10.1007/s00466-012-0702-1).
- [19] T. McComb. “Power scaling of large mode area thulium fiber lasers in various spectral and temporal regimes”. PhD thesis. University of Central Florida, 2009. URL: <https://stars.library.ucf.edu/etd/3975>.
- [20] J. M. Melenk, L. Demkowicz, and S. Henneking. “Stability analysis for electromagnetic waveguides. Part 1: Acoustic and homogeneous electromagnetic waveguides”. In: *SIAM Journal on Mathematical Analysis* 57.3 (2025), pp. 2559–2595. DOI: [10.1137/23M1599239](https://doi.org/10.1137/23M1599239).
- [21] J. Mora-Paz, S. Henneking, L. Demkowicz, and J. Grosek. “DPG finite element analysis of a vectorial envelope Maxwell formulation for bent waveguides and optical fibers”. In: *In preparation* (2025).
- [22] *NIST Digital Library of Mathematical Functions*. <https://dlmf.nist.gov/>, Release 1.2.4 of 2025-03-15. F. W. J. Olver, A. B. Olde Daalhuis, D. W. Lozier, B. I. Schneider, R. F. Boisvert, C. W. Clark, B. R. Miller, B. V. Saunders, H. S. Cohl, and M. A. McClain, eds.
- [23] J. F. Nye. *Physical Properties of Crystals: Their Representation by Tensors and Matrices*. New York: Oxford University Press, 1985. ISBN: 978-0198511656.

- [24] D. Pardo, L. Demkowicz, C. Torres-Verdin, and C. Michler. “PML enhanced with a self-adaptive goal-oriented *hp* finite-element method and applications to through-casing borehole resistivity measurements”. In: *SIAM Journal on Scientific Computing* 30.6 (2008), pp. 2948–2964. DOI: [10.1137/070689796](https://doi.org/10.1137/070689796).
- [25] D. Richardson, J. Nilsson, and W. Clarkson. “High power fiber lasers: Current status and future perspectives”. In: *Journal of the Optical Society of America* 27.11 (2010), B63–B92. DOI: [10.1364/JOSAB.27.000B63](https://doi.org/10.1364/JOSAB.27.000B63).
- [26] X. Roselló-Mechó, M. Delgado-Pinar, A. Díez, and M. V. Andrés. “Measurement of Pockels’ coefficients and demonstration of the anisotropy of the elasto-optic effect in optical fibers under axial strain”. In: *Optics Letters* 41.13 (2016), pp. 2934–2937. DOI: [10.1364/OL.41.002934](https://doi.org/10.1364/OL.41.002934).
- [27] Y. Takuma, M. Miyagi, and S. Kawakami. “Bent asymmetric dielectric slab waveguides: a detailed analysis”. In: *Applied Optics* 20.13 (1981), pp. 2291–2298. DOI: [10.1364/AO.20.002291](https://doi.org/10.1364/AO.20.002291).
- [28] H. Taylor. “Bending effects in optical fibers”. In: *Journal of Lightwave Technology* 2.5 (2003), pp. 617–628. DOI: [10.1109/JLT.1984.1073659](https://doi.org/10.1109/JLT.1984.1073659).

Disclaimers

This article has been approved for public release; distribution unlimited. Public Affairs release approval #AFRL-2025-5370. The views expressed in this article are those of the authors and do not necessarily reflect the official policy or position of the Department of the Air Force, of the Department of Defense, nor of the U.S. government.